Spring 5-19-2017

Numerical Drag Prediction of NASA Common Research Models Using Different Turbulence Models

Pan Du
Washington University in St. Louis

WASHINGTON UNIVERSITY IN ST. LOUIS

School of Engineering and Applied Science

Department of Mechanical Engineering and Material Science

Thesis Examination Committee:

Ramesh Agarwal, Chair

David Peters

Swami Karunamoorthy

Numerical Drag Prediction of NASA Common Research Models Using Different Turbulence Models

by
Pan Du

A thesis presented to
The School of Engineering and Applied Science
of Washington University in
partial fulfillment of the
requirements for the degree
of Master of Science

May 2017
St. Louis, Missouri

Table of Contents

List of Figures

List of Tables

Acknowledgements

First of all, I would like to thank my supervisor Professor Ramesh Agarwal. Since I joined the CFD lab, he has been treating me with great patience and kindness. He constantly gave me encouragement, which is really important to me to stick to my research. I will never forget his guidance in my academic life.

Also, I would like to thank Dr. Qiulin Qu. When I began to understand the project, I encountered lots of difficulties, such as how to use the CFD solver Fluent, how to generate a good mesh, etc. Dr. Qiulin Qu gave me lots of advice and helped me in getting familiar with the project sooner than I thought. Also, Dr. Tim Wary provided me plenty of resource and references for my research and helped me with the mesh. Dr. Xu Han and Junhui Li gave me suggestions on improving the quality of my mesh and fixing the divergence in the solutions in many cases. I would like to sincerely thank all these people mentioned above as well as other students in the CFD lab.

I would also like to acknowledge my committee members, Dr. Peters and Dr. Karunarmoorthy, for taking the time to read the thesis and attend its defense.

Pan Du

Washington University in St. Louis

May 2017

Dedicated to my parents

I want to dedicate my thesis to my dear parents (Mrs. Fanghua Du and Mr. Lin Du) and my other family members for their guidance, love and support.

ABSTRACT OF THE THESIS

Numerical Drag Prediction of NASA Common Research Models Using Different Turbulence Models

by

Pan Du

Master of Science in Department of Mechanical Engineering and Material Science

Washington University in St. Louis, 2017

Research Adviser: Professor Ramesh Agarwal

The goal of this research is to perform 3D turbulence flow simulations to predict the drag of Wing-body-tail (WBT) and Wing-body-nacelle-Pylon (WBNP) aircraft configurations from NASA Common Research Models. These configurations are also part of the 4th and 6th AIAA Drag Prediction Workshops in which CFD modelers have participated worldwide. The computations are performed using CFD solver ANSYS FLUENT. The compressible Reynolds-Averaged Navier-Stokes (RANS) equations are solved using two turbulence models – the Spalart-Allmaras (SA) and SST k-ω. Drag polar and drag rise curves are obtained by performing computations at different angles of attack at a constant Mach number. Pressure distributions and flow separation analysis are presented at different angles of attack. Comparison of computational results for WBT and WBNP models is made with the experimental data using the two turbulence models; good agreements is obtained. For WBNP, an aero-elastically deformed model of the wing is also

considered at an angle of attack of 2.75°; the computations again are in reasonable agreement with the experiment. The computed WBNP results are compared with WB results for the drag increment study.

Chapter 1: Introduction

In this Chapter, the motivation behind this study and the background of the project are presented. It also introduces the outline of the thesis and a summary of the related published results in the literature, which primarily come from the AIAA Drag Prediction Workshops. The scope of the thesis is also included.

1.1 Motivation

A great deal of effort has been devoted over past several decades to obtain the accurate numerical solutions for flow past a transonic commercial aircrafts and other aerospace industry relevant configurations using the tools of Computational Fluid Dynamics (CFD). The accuracy of drag prediction has been the most challenging among all the aerodynamic coefficients. There has been rapid progress in the improvement of CFD tools namely the geometry modeling, grid generation, numerical algorithms and turbulence modeling for accurate and efficient solution of Reynolds-Averaged Navier-Stokes (RANS) equations for the flow field of almost complete aircraft configurations; however the turbulence modeling remains a challenging task which has major influence on the accuracy of drag prediction because of relatively small magnitude of drag coefficient compared to the lift coefficient. Nevertheless, at present the accuracy of cruise drag prediction of an aircraft from CFD is claimed to be within 1% range of the theoretical solution [1]. Since 2001, a series of drag prediction workshops have been organized by the AIAA Applied Aerodynamics Technical Committee [2]. The main purpose of the workshops has been to assess the state-of-the art computational technology as a tool for drag, lift and moment predictions of aircrafts. The DPW (Drag Prediction Workshop) has established a platform for aerodynamics

researchers from academia, industry and government labs to communicate, exchange ideas and compare results by using different meshes, turbulence models and flow solvers.

There are many CFD solvers that have been developed worldwide by the commercial CFD vendors (e.g. ANSYS FLUENT, CFD++, CFX, STAR-CD, COMSOL etc.), and by the industry (e.g. Boeing BCFD, German Tau etc.) and the government labs (e.g. FUN3D, OVERFLOW, CFL3D, TLNS3D, COBALT, WIND etc.), and the open source software OpenFOAM that differ in mesh generation capability and numerical algorithms and in available suite of turbulence models. This list is not inclusive of all the solvers that are currently in use in the CFD community. Many of these solvers have been used in solving the flow field of NASA research models identified in DPW4 and DPW6.

It has been pointed out by many investigators that a turbulence model plays an important role in drag prediction considering other numerical aspects of various codes such as mesh generation and numerical algorithms being almost similar. The motivation behind this study is to assess the relative accuracy of same widely used turbulence models by computing the flow fields of two NASA Common Research Models namely the Wing-Body-Tail (WBT) and Wing-Body-Nacelle-Pylon (WBNP) from 4th and 6th AIAA Drag Prediction Workshops, respectively.

1.2 Brief Review of Literature

Since the beginning of AIAA Drag Prediction Workshops, a great deal of research has been conducted on the aerodynamic and flow field analysis of NASA Common Research Models by computational and experimental means. Mavriplis and Long employed the NSU3D solver from NASA using both the SA and standard k-ω turbulence models and found that their results are in close agreement with the collection of other results from the 4th AIAA Drag Prediction Workshop

[3]. Sclafani and Mark DeHaan employed the CFL3D solver with SA turbulence model and OVERFLOW solver with both SA and SST k-ω models to study the downwash as well as the drag polar of the NASA Common Research Model. They showed that the two equations SST *k*-ω model predicts a stronger shock on the wing than the one equation SA model [4]. Morrison performed the statistical analysis of the results from an extensive N-version test of a collection of Reynolds-Averaged Navier–Stokes (RANS) codes in response to the 4th generation of AIAA DPW. The results showed that the total drag, pressure drag and skin friction drag decreased as the grid resolution increased [5]. Mani and Rider from Boeing company led the research on computational analysis of DPW4 using the CFL3D (block structured), OVERFLOW (overset structured), and BCFD (unstructured)codes. They reached a conclusion that the three codes showed great consistency with other results in DPW4; the application of advanced grid adaption methods ensured accurate solutions on less-than-finest initial grids [6].

1.3 Scope of This Thesis

The Scope of the thesis is to conduct the computational study of the aerodynamics and flow fields of two NASA Common Research Models, WBT and WBNP from AIAA 4th and 6th Drag Prediction Workshops respectively using various turbulence models and compare the results with the experimental data and the computational results from other participants in the workshop. For WBNP, an aeroelastically deformed model of the wing is also considered.

Chapter 2: Methodology

In this section, the three configurations of NASA common research models (Wing-body ae2.75, Wing-body-tail (WBT) and Wing-body-nacelle-pylon (WBNP) are introduced. The structured mesh and turbulence models are also introduced.

2.1 Geometries of WBT and WBNP

Two geometries from NASA Common Research Model are computed and analyzed in this thesis: The Wing-body-Tail (WBT) from 4th Drag Prediction Workshop and the Wing-body-Nacelle-Pylon (WBNP) from 6th Drag prediction workshop [7] as shown Fig 2.1 and Fig 2.2, respectively.

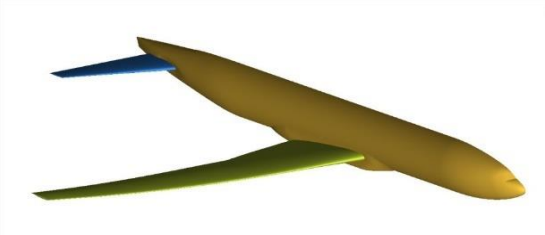

Fig 2.1 WBT configuration

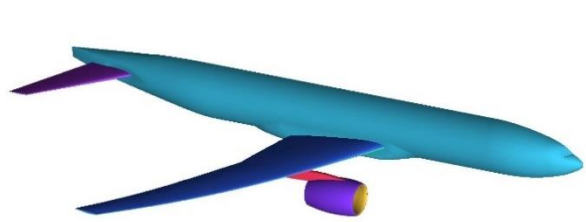

Fig 2.2 WBNP configuration

Geometric parameters for these two configurations are given in Table 2.1.

Table 2.1 Geometric parameters for WBT and WBNP

Parameters	WBT	WBNP
S_{ref}/in^2	594.72	594.72
C_{ref}/in	275.8	275.8
$T_{ref}/°F$	100	100
AR	9	9
b/in	2313.4	2313.4
M	0.85	0.85
Re× 10^6	5	5
AoA/°	0°,1°,2°,2.38°,2.5°,3°,4°	0°,1°,2°,2.75°,3°,4°

2.2 Mesh Generation

2.2.1 WBT Mesh

ICEM CFD in ANSYS is used for geometry modeling and mesh generation. A structured mesh is used for both the configurations, since the structured mesh requires less memory. Fig 2.3 shows the computation domain for WBT. The shape of the far field is a cuboid, which consists of an outlet surface, a symmetry surface and the far field. Assuming the length of the fuselage normalized as l, the length of the far field is 200. The WBT/WBNP configuration is located at the center of the bottom surface of the far field. Fig 2.3 shows both the computational domain and the

mesh in the far field for WBT configuration. Fig 2.4 shows the structure mesh around the WBT configuration. Using the NASA calculator, the height of first mesh layer h = 0.00098 in. The first layer of mesh adjacent to the model boundary surface satisfies the condition y+ < 1. Thus, for application of SST *k-ω* turbulence model, there are enough layers of meshes inside the viscous sublayer to obtain good resolution of the turbulent boundary layer profile. T/ guarantee the accuracy of the computational result, there are several other requirements are addressed in building the mesh: the chord-wise spacing is kept below 0.1% of the chord for meshes on both the lower and upper surfaces, and near the leading and tailing edge of both the wing and the horizontal tail; spacing at the root and tip of the wing and tail is below 0.1% of the semi-span; the mesh size at nose of the fuselage is smaller than 2% of C_{ref} [8]. The total number of nodes for this mesh is around 11 million. It can be considered as medium level mesh for DPW4 based on the information from AIAA DPW4.

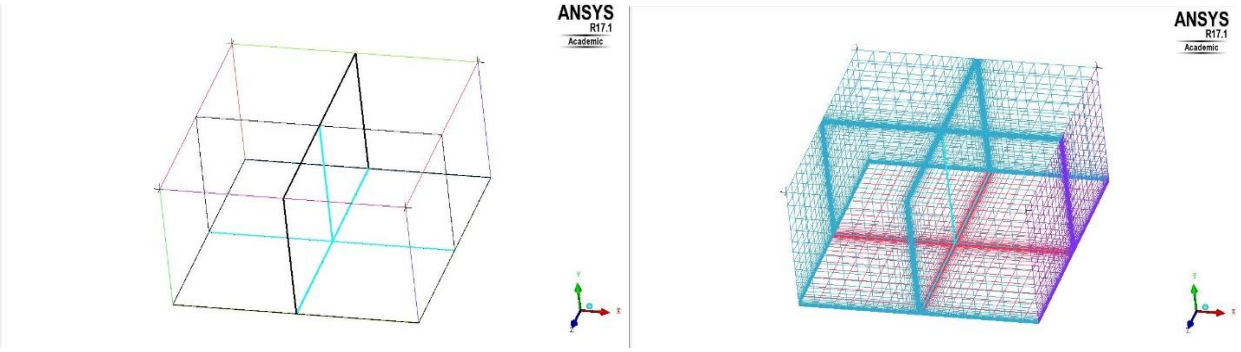

Fig 2.3 3D view of cubic computational domain with structured mesh in the far field for WBT

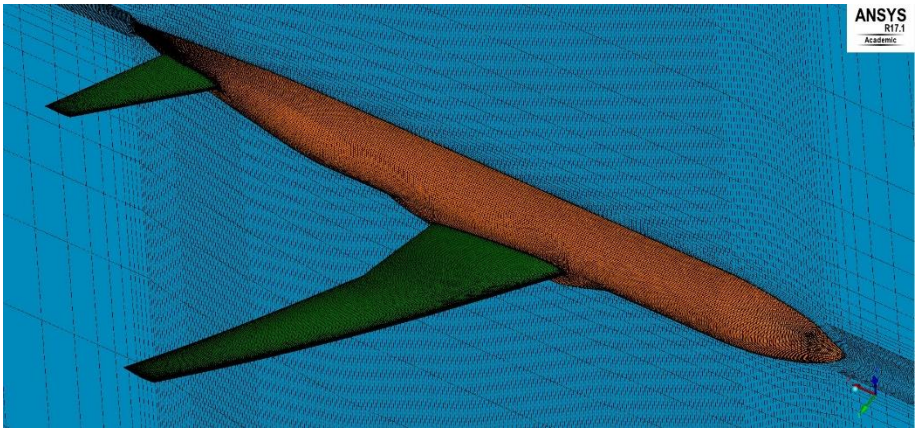

Fig 2.4 3D structured mesh around WBT

2.2.2 WBNP Mesh

Fig 2.5 shows the computational domain for WBNP configuration; it is a half sphere. It shows both the computational blocks and the mesh shells on WBNP. Fig 2.6 shows the structured mesh around the WBNP configuration. The total number of nodes of in this mesh is around 12 million. The far field of the sphere is about the same size as the far field of WBT configuration. Due to addition of nacelle and pylon, the mesh quality behind the nacelle and around the pylon is not as high as desired, which results in higher residuals in computations when compared to the WBT cases. However, the computational results are still of reasonable accuracy.

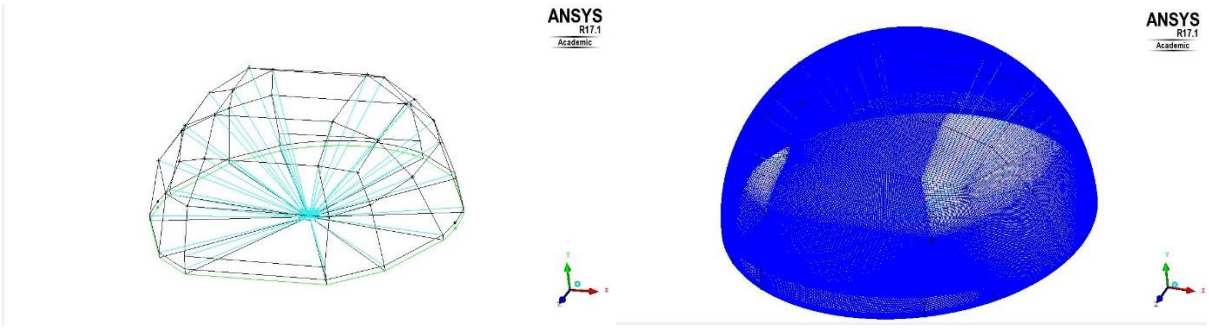

Fig 2.5 3D view of a hemi-spherical computational domain with structured mesh for WBNP

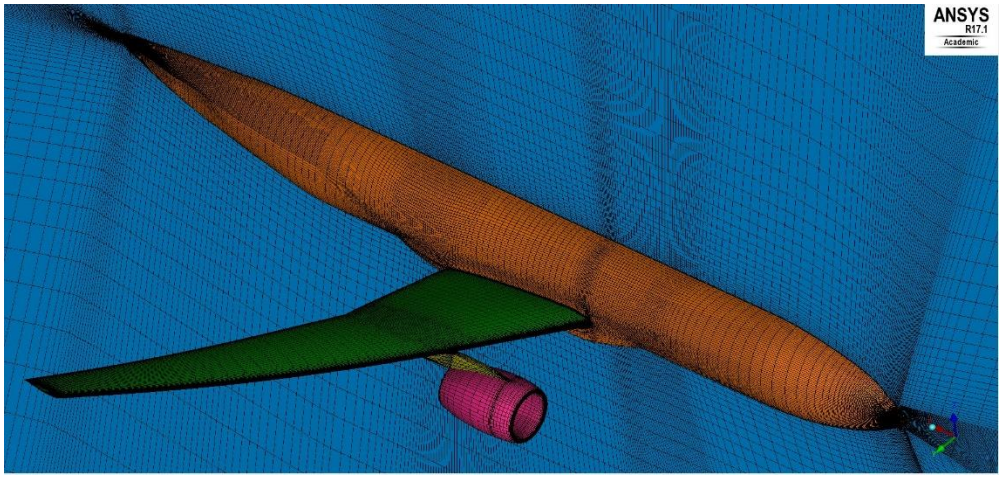

Fig 2.6 3D structured mesh around WBNP

2.2.3 WB ae2.75 Mesh

Fig 2.7 shows the WB ae2.75 computational domain. Both computational blocks and mesh shells are displayed. The cubic mesh is around 11 million nodes. Fig 2.8 shows the detailed mesh around WB aeroelastic configuration. The mesh structure is similar to the mesh for WBT configuration. The results for WB aeroelastic configuration are compared to the results for WBNP configuration for drag increment study.

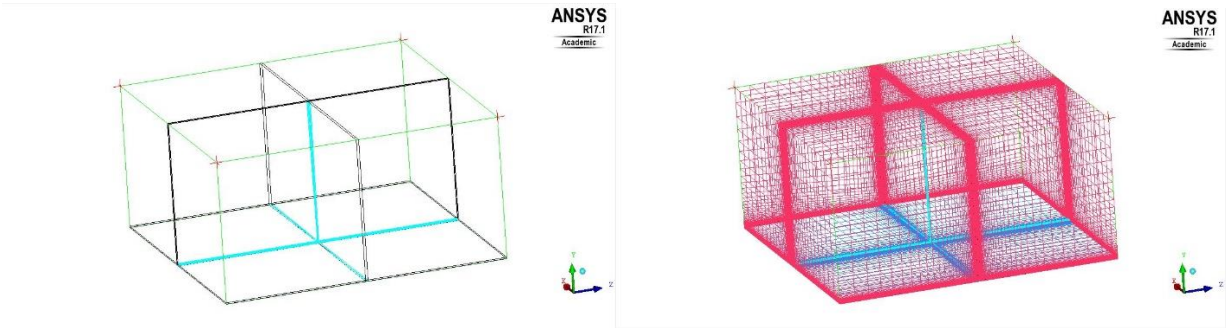

Fig 2.7 3D view of computational domain with structured mesh for WBae2.75

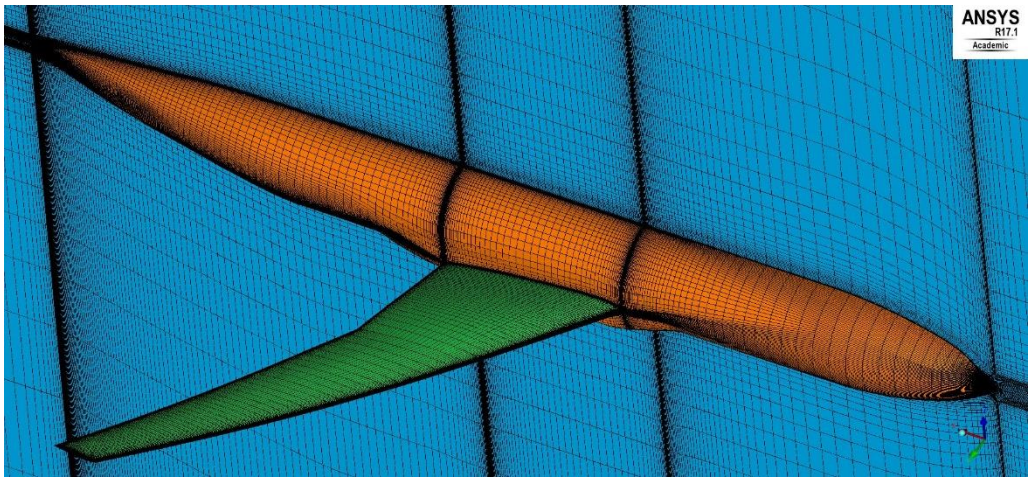

Fig 2.8 3D structured mesh around WB ae2.75

2.3 Simulation Method

Computations are performed using the CFD software Fluent 17.1. Steady compressible Reynolds-Averaged Navier-Stokes (RANS) equations are solved using the finite volume method. Both Spalart-Allmaras (S-A) and k-ω SST two-equation model are used in the study. A second order upwind scheme is used for the convection terms and a second order central difference scheme is used for the diffusion terms. For cases of WBT, WBNP and WBae2.75 configurations, SIMPLE algorithm is employed for pressure-velocity coupling. The Computed solution is uploaded in CFD post for analysis of the numerical data.

2.4 Turbulence Models

The Spalart-Allmaras (SA) model is the most widely used turbulence model for simulations. It has been applied extensively to compute the aerodynamics problems with turbulent boundary layers. It has shown ability to compute adverse pressure gradient flows with reasonable accuracy. It is more likely to converge quicker compared to the k-ω SST model and is more efficient being a one-equation model [9].

2.4.1 Spalart-Allmaras (SA) Model

The standard SA model is governed by the following equation:

$$\frac{\partial \hat{v}}{\partial t} + u_j \frac{\partial \hat{v}}{\partial x_j} = c_{b1}(1 - f_{t2})\hat{S}\hat{v} - [c_{w1} f_w - \frac{c_{b1}}{\kappa^2} f_{t2}](\frac{\hat{v}}{d})^2 + \frac{1}{\sigma}[\frac{\partial}{\partial x_j}((v + \hat{v})\frac{\partial \hat{v}}{\partial x_j}) + c_{b2}\frac{\partial \hat{v}}{\partial x_i}\frac{\partial \hat{v}}{\partial x_i}]$$

The turbulent eddy viscosity is computed from:

$$\mu_t = \rho \hat{v} f_{v1}$$

where

$$f_{v1} = \frac{X^3}{X^3 + c_{v1}^3}$$

$$X = \frac{\hat{v}}{v}$$

In above equation, ρ denotes density. μ denotes the molecular dynamic viscosity and $v = \mu / \rho$ denotes the molecular kinetic viscosity.

Other definitions of variables are:

$$\hat{S} = \Omega + \frac{v}{\kappa^2 d^2} f_{v2}$$

where $\Omega = \sqrt{2W_{ij}W_{ij}}$ is the magnitude of vorticity.

$$f_{v2} = 1 - \frac{X}{1 + X f_{v1}} \qquad f_w = g[\frac{1 + c_{w3}^6}{g^6 + c_{w3}^6}]^{1/6}$$

$$g = r + c_{w2}(r^6 - r)$$

$$r = \min[\frac{\hat{v}}{\hat{S}\kappa^2 d^2}, 10]$$

$$f_{t2} = c_{t3} \exp(-c_{t4} X^2)$$

$$W_{ij} = \frac{1}{2}(\frac{\partial u_i}{\partial x_j} - \frac{\partial u_j}{\partial x_i})$$

Boundary conditions are:

$$\hat{v}_{wall} = 0$$

$$\hat{v}_{farfield} = 3v_\infty : to : 5v_\infty$$

The kinematic eddy viscosity values at wall and in the far field are:

$$v_{t,wall} = 0$$

$$v_{t,farfield} = 0.210438v_\infty : to : 1.294234v_\infty$$

The model constants are:

$$c_{b1} = 0.1355 \qquad \sigma = 2/3 \qquad c_{b2} = 0.622 \qquad \kappa = 0.41$$

$$c_{w2} = 0.3 \qquad c_{w3} = 2 \qquad c_{v1} = 7.1 \qquad c_{t3} = 1.2 \qquad c_{t4} = 0.5$$

$$c_{w1} = \frac{c_{b1}}{\kappa^2} + \frac{1 + c_{b2}}{\sigma}$$

2.4.2 SST k-ω Model

Unlike the SA model, the *k*-ω SST model is governed by two equations. This model is more complex than SA model and requires more computational cost for simulation. It also relies on the distance to the wall [10].

The governing equations are:

$$\frac{\partial(\rho k)}{\partial t}+\frac{\partial(\rho u_j k)}{\partial x_j}=P-\beta^*\rho\omega k+\frac{\partial}{\partial x_j}[(\mu+\sigma_k\mu_t)\frac{\partial k}{\partial x_j}]$$

$$\frac{\partial(\rho\omega)}{\partial t}+\frac{\partial(\rho u_j \omega)}{\partial x_j}=\frac{\gamma}{\nu_t}P-\beta\rho\omega^2+\frac{\partial}{\partial x_j}[(\mu+\sigma_\omega\mu_t)\frac{\partial\omega}{\partial x_j}]+2(1-F_1)\frac{\rho\sigma_{\omega 2}}{\omega}\frac{\partial k}{\partial x_j}\frac{\partial\omega}{\partial x_j}$$

P is defined as:

$$P=\tau_{ij}\frac{\partial u_i}{\partial x_j}$$

$$\tau_{ij}=\mu_t(2S_{ij}-\frac{2}{3}\frac{\partial u_k}{\partial x_k}\delta_{ij})-\frac{2}{3}\rho k\delta_{ij}$$

$$S_{ij}=\frac{1}{2}(\frac{\partial u_i}{\partial x_j}+\frac{\partial u_j}{\partial x_i})$$

The turbulent eddy viscosity is computed from:

$$\mu_t=\frac{\rho a_1 k}{\max(a_1\omega,\Omega F_2)}$$

Inner and outer constant are combined as:

$$\phi = F_1\phi_1 + (1 - F_1)\phi_2$$

where:

$$F_1 = \tanh(\arg_1^4)$$

$$\arg_1 = \min[\max(\frac{\sqrt{k}}{\beta^* \omega d}, \frac{500\nu}{d^2\omega}), \frac{4\rho\sigma_{\omega 2}k}{CD_{kw}d^2}]$$

$$CD_{kw} = \max(2\rho\sigma_{\omega 2}\frac{1}{\omega}\frac{\partial k}{\partial x_j}\frac{\partial \omega}{\partial x_j}, 10^{-20})$$

$$F_2 = \tanh(\arg_2^2)$$

$$\arg_2 = \max(2\frac{\sqrt{k}}{\beta^* \omega d}, \frac{500\nu}{d^2\omega})$$

$\Omega = \sqrt{2W_{ij}W_{ij}}$ is the magnitude of vorticity:

$$W_{ij} = \frac{1}{2}(\frac{\partial u_i}{\partial x_j} - \frac{\partial u_j}{\partial x_i})$$

Boundary conditions are:

$$\frac{U_\infty}{L} < \omega_{farfield} < 10\frac{U_\infty}{L}$$

$$\frac{10^{-5}U_\infty^2}{\mathrm{Re}_L} < k_{farfield} < \frac{0.1U_\infty^2}{\mathrm{Re}_L}$$

$$\omega_{wall} = 10\frac{6\nu}{\beta_1(\Delta d_1)^2}$$

$$k_{wall} = 0$$

The model constants are:

$$\gamma_1 = \frac{\beta_1}{\beta^*} - \frac{\sigma_{\omega 1}\kappa^2}{\sqrt{\beta^*}} \qquad \gamma_2 = \frac{\beta_2}{\beta^*} - \frac{\sigma_{\omega 2}\kappa^2}{\sqrt{\beta^*}}$$

$$\sigma_{k1} = 0.85 \qquad \sigma_{\omega 1} = 0.5 \qquad \beta_1 = 0.075$$

$$\sigma_{k2} = 1.0 \qquad \sigma_{\omega 2} = 0.856 \qquad \beta_2 = 0.0828$$

$$\beta^* = 0.09 \qquad \kappa = 0.41 \qquad a_1 = 0.31$$

Chapter 3: Analysis of WBT from DPW4

In this Chapter, the computational analysis of WBT configuration from 4th AIAA Drag Prediction Workshop (DPW4) is presented using different turbulence models. The computations are compared with experimental data and with the computations of other participants in the workshop.

3.1 Drag Polar Analysis

The results are presented in Figs. 3.1-3.4. In these figures, 'sst0' labeled results are from Oswald's results obtained using ANSYS [8], 'exp' denotes the experiment results from a wind tunnel test on a scaled model at the same Reynolds number and Mach number [11], and 'sa' and 'sst' denote the present computational results obtained with SA model and SST k-ω model, respectively. Figure 3.1 shows the comparison of results for the lift coefficient at various angles of attack α. Present SA and SST results are quite close to those of Oswald from α = 0° to 4°. The slope of the lift curve at small angles of attack is about k = 0.146 deg^{-1}. The rate of increase in slope becomes smaller as α becomes greater than 2.5° due to flow separation. Both computational results obtained with SA and SST model are in reasonable agreement with the experimental data. In wind tunnel experiment, errors can be generated due to vibration of aircraft model, boundaries of the wind tunnel, and gas pulsation, etc. There still exist differences between the numerical simulation and the experiment data although corrections have been added to the wind tunnel results. The maximum of absolute error between the experimental results and the computations with SST model is e_m = 0.094. Figure 3.2 shows the drag coefficient as a function of α. Similar to the lift curve, computational results show reasonable agreement with the experimental data when α < 3°. However, when α = 4°, the results from SST model are much higher with a value of 0.06. This large discrepancy in the computation and experiment implies that the prediction of flow near the

surface of the wing and the horizontal tail where the streamline curvature varies a great deal becomes inaccurate for this mesh using the SST k-ω turbulence model when α is high. This might also be caused by lack of mesh resolution in the boundary layer region. The experimental drag coefficient curve is significantly below the computational curve. The maximum absolute error between experimental results and the computational results with SST k-ω model is e_m =0.024. As shown in Fig. 3.3, similar pattern appears in the result; C_l vs. C_d curve of computational results are consistent. But there exists small error between the experimental results and computational results.

Figure 3.4 shows the idealized drag polar. It can be observed that the difference between the experiment and computation with SST k-ω model can again be explained as before in case of Figs. 3.3 and 3.4. The curves of drag polar are similar except at the last point obtained from computation using the SST k-ω model (this corresponds to the calculation at α = 4°). As for the idealized drag polar in Fig 3.4, computational results in general are in good agreement at low values of C_l. The experimental curve is slightly left of the computational curve. In Fig. 3.5, it appears that the pitching moment turns to be negative when the angle of attack reaches approximately 2.5°. From data 'sst1', 'sst2' and 'sa0' (all published data from DPW4), one can conclude that some of those simulation results exhibit a twist in pitching moment at large angle of attack (AoA=4°), but some do not. Actually the trend of the lift-pitching moment curve depends on the quality and the type of the grids as well as the turbulence models. As for 'sa' and 'sst' data obtained by the author, the curve doesn't show any increase at the end.

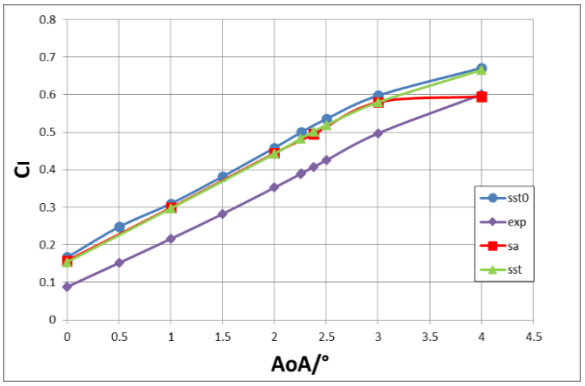

Fig 3.1 Lift coefficient vs. α curve for WBT

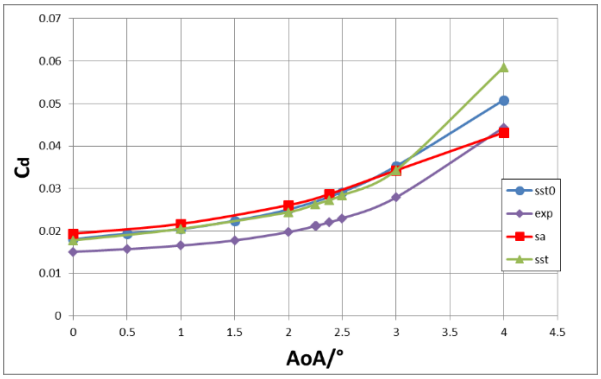

Fig 3.2 Drag coefficient vs. α curve for WBT

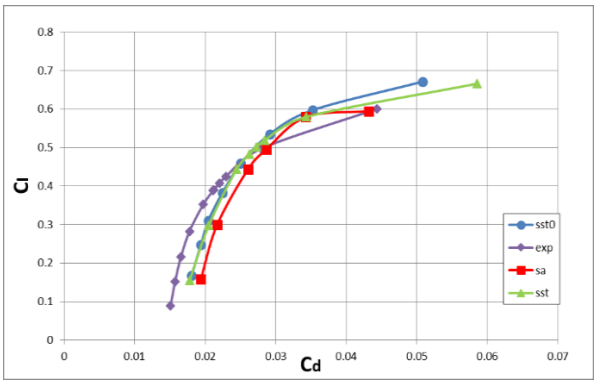

Fig 3.3 C_l vs. C_d curve for WBT

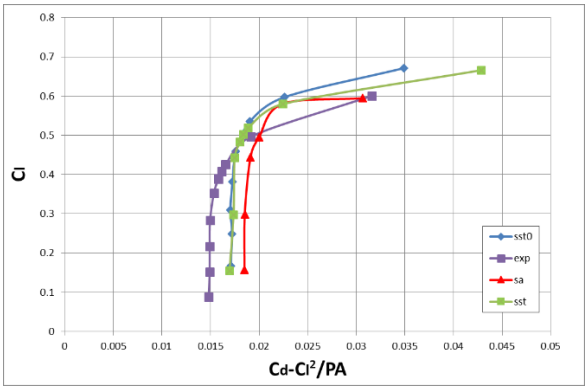

Fig 3.4 Idealized drag polar

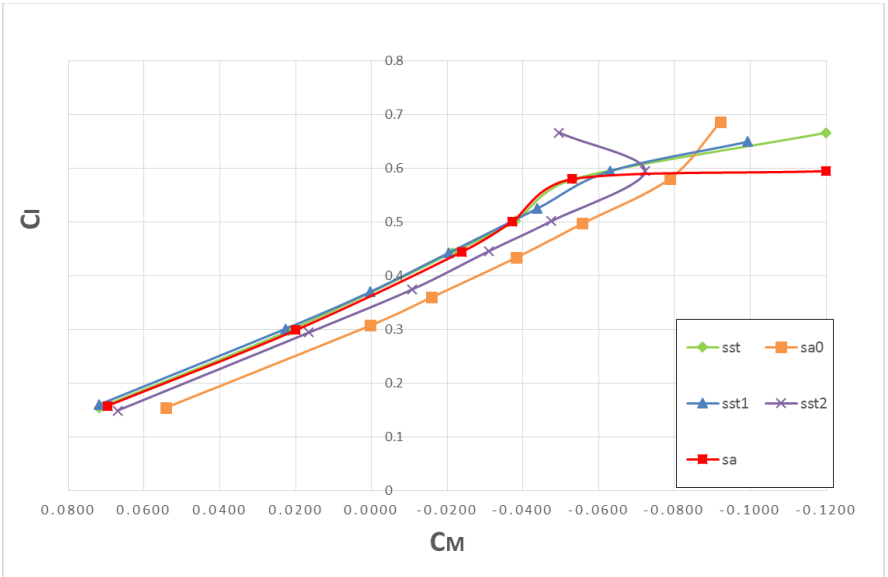

Fig 3.5 Pitching moment

3.2 Pressure Distribution at Various Cross-Sections of WBT

Figure 3.6 shows the location of various cross sections at wing-root, wing mid-span and wing-tip where the present computed pressure distributions are compared with those obtained from OVERFLOW [11] as required by DPW4. In addition, there is also a cross section at horizontal tail. The comparisons are done for the case of C_l = 0.5. In order to determine the angle of attack for C_l = 0.5, C_l was computed at α = 0°,1°, 2°, 2.5° ,3°, and 4°. The angle of attack where C_l=0.5 was determined from this curve. For this angle of attack, C_l was again computed to verify that its value was indeed = 0.5. It was finally determined that C_l = 0.5 at α =2.38°. All the pressure distributions are compared for C_l=0.5. Figure 3.7 shows the comparison of present computed pressure distributions on four sections of the wing using the SST k-ω model with those computed by OVERFLOW using the SA model; excellent agreement is obtained. Figure 3.8 shows the comparison of pressure distribution on a section on the tail. Again, excellent agreement is obtained.

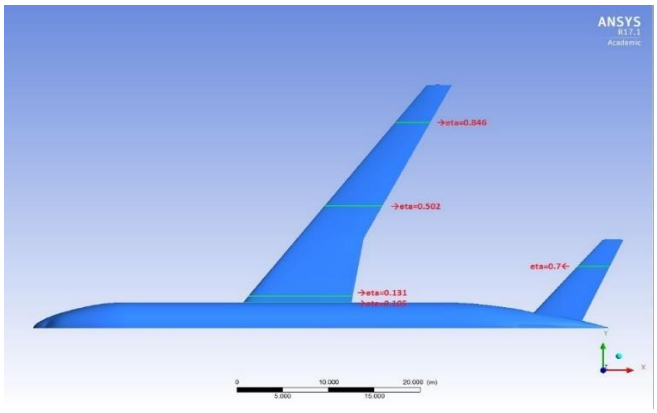

Fig 3.6 Cross sections at the wing and the tail for comparison of pressure distribution

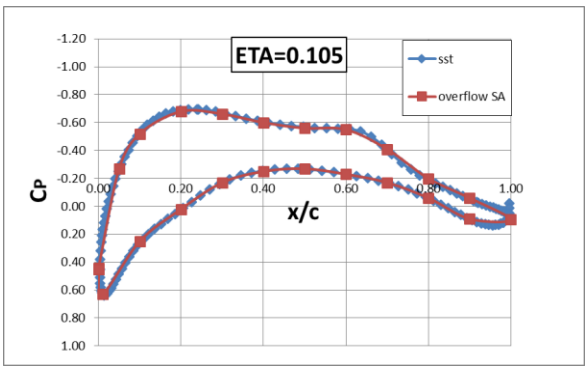

(a)

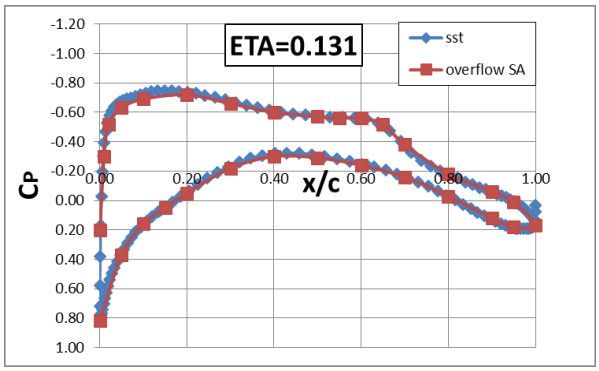

(b)

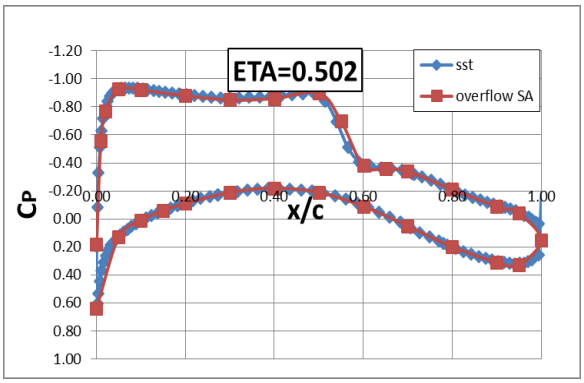

(c)

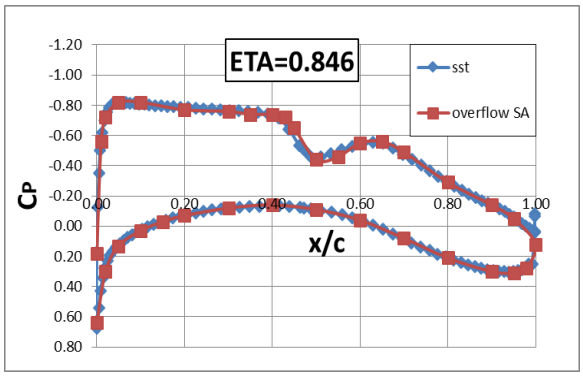

(d)

Fig 3.7 Comparison of computed pressure distributions at four cross-sections on the wing between the present results using ANSYS FLUENT with SST k-ω model and OVERFLOW code with SA model

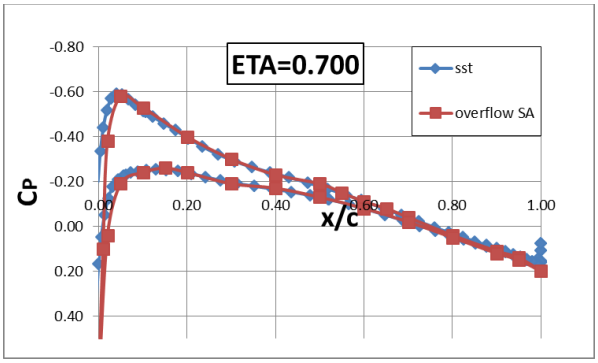

Fig 3.8 Comparison of computed pressure distributions at a cross-section on the tail between the present results using ANSYS FLUENT with SST model and OVERFLOW code with SA model

Figure 3.8 shows the pressure contours on the WBT. Figure 3.9 (a) and 3.9 (b) show the view in -z and +z direction respectively. Figure 3.9 (c) shows the three-dimensional view. The C_P on the leading edge is lower than that on the trailing edge on the upper surface of wing and the horizontal tail. C_P on the lower surface of the wing is larger than that on the upper surface of the wing as expected. The change of pressure is much smaller on the horizontal tail than that on the wing. Pressure also increases at the fuselage near the junction between the wing and the fuselage. The maximum of pressure appears at the nose of the fuselage due to stagnation point.

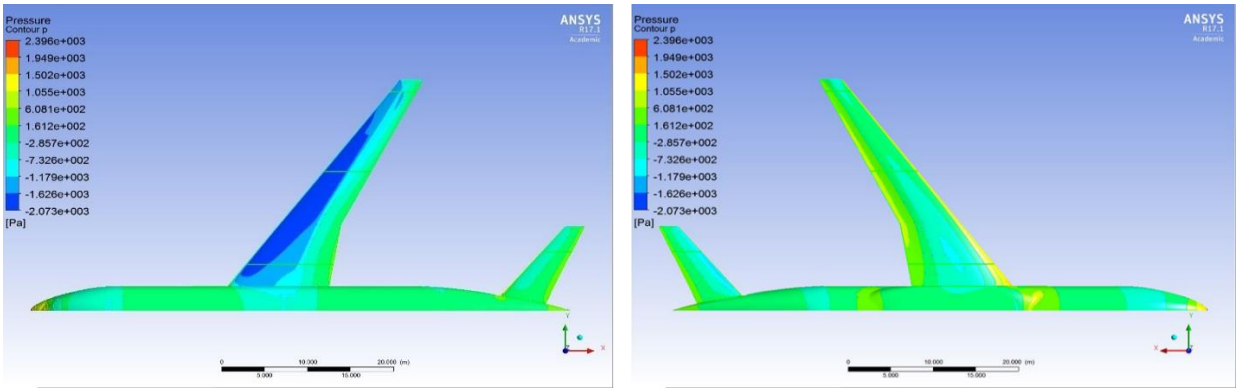

(a) (b)

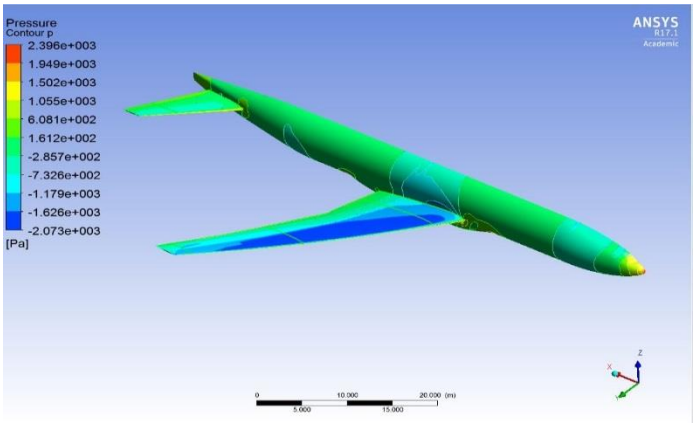

(c)

Fig 3.9 Computed pressure contours using ANSYS FLUENT with SST k-ω model

3.3 Flow Separation

Accurate computation of flow separation is considered very important in drag prediction of configurations in DPW series [12]. Normally there are three parts where separation might occur in WBT flow simulation: 1) the corner near trailing edge next to the fuselage, 2) the trailing edge separation at wing and tail and 3) the tail-body juncture region [4]. As shown in Fig. 3.10, the stream line curvature is large at the juncture of fuselage and wing near the trailing edge. One can clearly see a 3D separation bubble near wing body juncture projecting streamlines to both surfaces, which is in good agreement with the results presented in DPW4. The length and the width of the separation bubble are measured in the SST model case (noted in Fig.14). Table 3.1 shows the results, where C_{ref} is reference length.

Table 3.1 Separation bubble parameters

Parameters	Wing root bubble	Separation pocket near tail
ΔBL/in	4.921	7.787
ΔBL/ C_{ref}	1.784%	2.823%
ΔFS/in	19.68	25.88
ΔFS/ C_{ref}	7.137%	9.384%
Platform size/in2	96.8751	201.5526

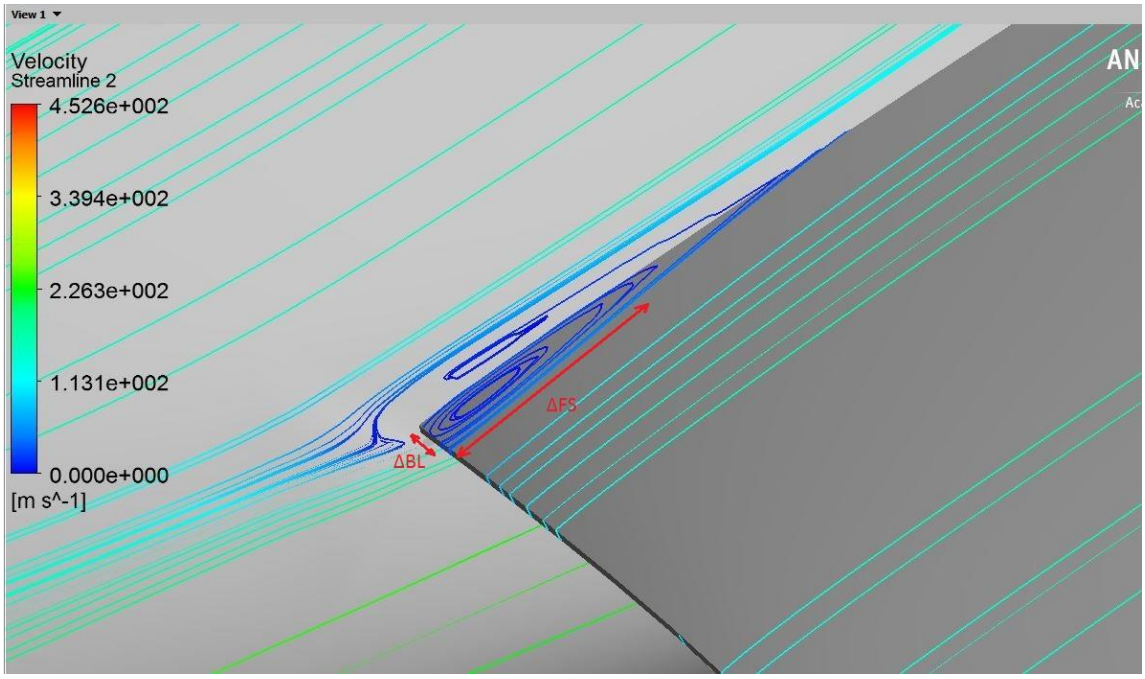

(a) Wing root separation bubble

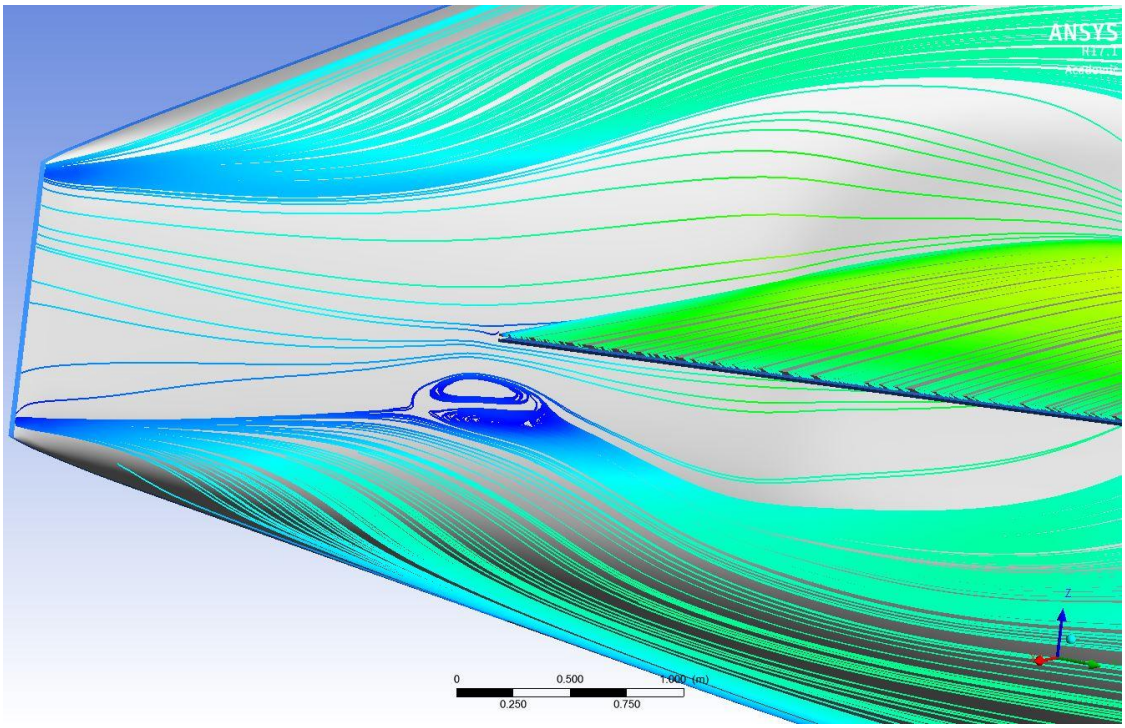

(b) Separation pocket near tail

Fig 3.10 Flow separation at the wing-body junction near the wing trailing edge

From Table 3.1, bubble length and width is 7.137% and 1.784% of reference length respectively. It's within reasonable range of percentage for the size of separation bubble. There exists separation near wing fuselage juncture when angle of attack is 2.38°. As shown in Fig.14, the separation pocket is well defined in 10 million level grid solution. The result shows that the plan size of the pocket is bigger than the separation bubble at the wing root.

3.4 Conclusions

In conclusion, for drag and lift coefficient on WBT configuration, results of SA and *k*-ω SST models are very close, and they are consistent with the k-ω SST results published in DPW4. However, there exists small error between the simulations and experimental results. The experimental result is obtained from wind tunnel conditions, where the flow is restricted inside four walls and the wing is going through change in shape due to aeroelastic effect. There is also a frame used to support the aircraft model. All these factors can cause differences between the wind tunnel and simulation results. The drag coefficient obtained in the present simulations using the *k*-ω SST model appears to be inaccurate due to the resolution of the mesh.

The pressure distribution results of OVERFLOW SA and the SST are consistent at all sections of the wing and tail. The magnitude of the pressures and the shock locations are also consistent.

There is flow separation at the juncture of wing and fuselage near the trailing edge. The length, width and the plan size of separation bubble is within reasonable range. A separation pocket is observed below the tail on the fuselage. The separation pocket is well defined at this level of resolution with the SST k-ω model. The plan size appears to be bigger than the separation bubble at the wing fuselage juncture.

Chapter 4: Analysis of WBPN from DPW6

In this section, the flow field of wing-body-nacelle-pylon (WBNP) configuration is compared. The flow conditions are obtained from the 6th AIAA Drag Prediction Workshop.

4.1 Lift and Drag Coefficients and Drag Polar

Figure 4.1 shows the comparison of computed results for C_l, C_d and drag polar from FLUENT using SST k-ω model, results from NASA FUN3D code and experimental data. FUN3D results are obtained from the work of Abdol-Hamid et al. reported on AIAA DPW6 website [13]. The geometry used in this paper is the aero elastic model at α = 2.75°, which is different from the original shape of the model. The high angle of attack can lead to deformation of the wing due to aero-elasticity which can cause the position of the tip of the wing to change [14]. The computations for this configuration are performed for α = 0° to 4° and are compared with the experimental data. It appears that C_l computed from FLUENT with SST k-ω model and FUN3D is in good agreement with the experimental data. The maximum difference in C_l between the FLUENT result and experimental result is e_m = 0.02918. The lift curve slope is k = 0.1318 deg^{-1}. The computational results for C_d are also in acceptable agreement with the wind tunnel results. Maximum error in C_d between the wind tunnel data and the FLUENT calculation is e_m =0.01218. For the drag polar in Fig. 4.1 (c), the computational results move slightly to the right of the experimental drag polar but are within the acceptable range. However, FUN3D results are always closer to the FLUENT results. For the idealized drag polar shown in Fig. 4.1 (d), the error seems to be getting bigger at higher angles of attack, the prediction error is relatively large at high angle of attack.

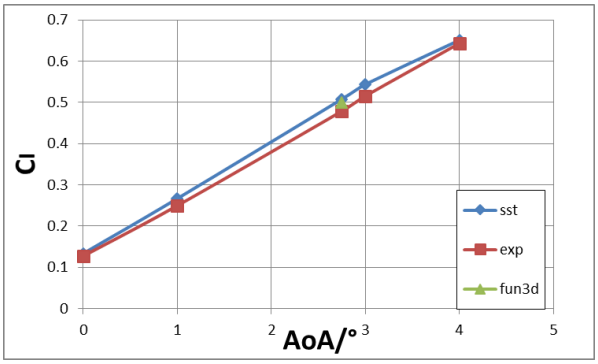

(a) Lift coefficient vs. angle of attack

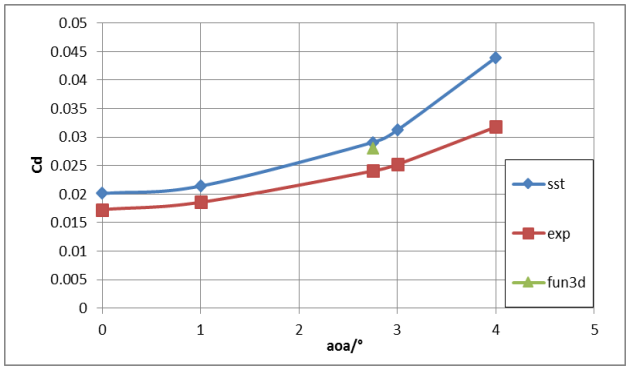

(b) Drag coefficient vs. angle of attack

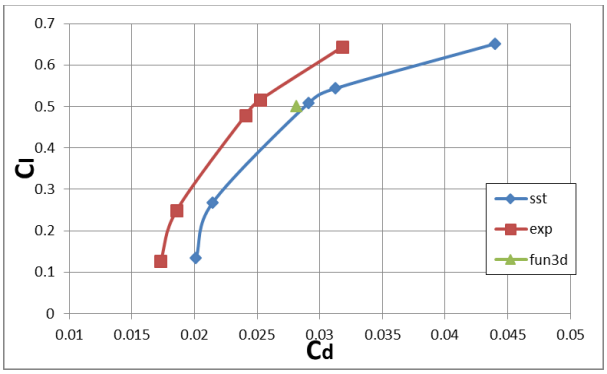

(c) Drag polar

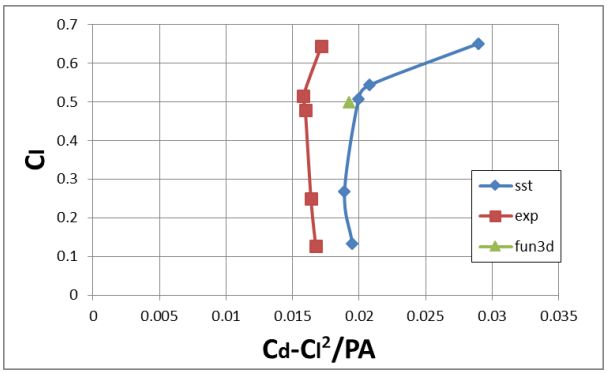

(d) Idealized drag polar

Fig 4.1 Lift, drag and drag polar for WBNP

4.2 Pressure Distribution on Various Cross-Sections of the Wing

Figure 4.2 shows the comparison of computed pressure distribution using FLUENT with SST k-ω model and those from overset grid solver. One can see that the predictions are generally close to the overset results presented in DPW6 [15]. At ETA = 0.131 and 0.283, the SST k-ω model pressure distributions agree well near the leading edge and trailing edge but have small error over the rest of the chord-wise location when compared to the overset result. Also, at the cross section moving towards the middle of the wing, the shock becomes more manifest and the pressure difference between the upper and the lower surface of the wing increases. At ETA= 0.603, there is excellent agreement between the SST k-ω and overset results except that the locations where the first shock ends have small difference. But the error is within reasonable range. The overall shape and maximum and minimum value of pressure are also consistent between the two results.

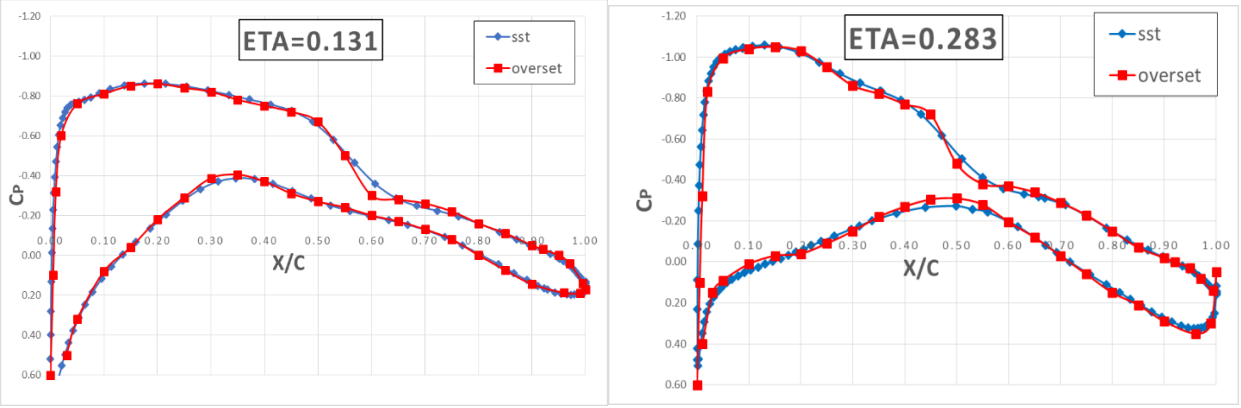

(a) (b)

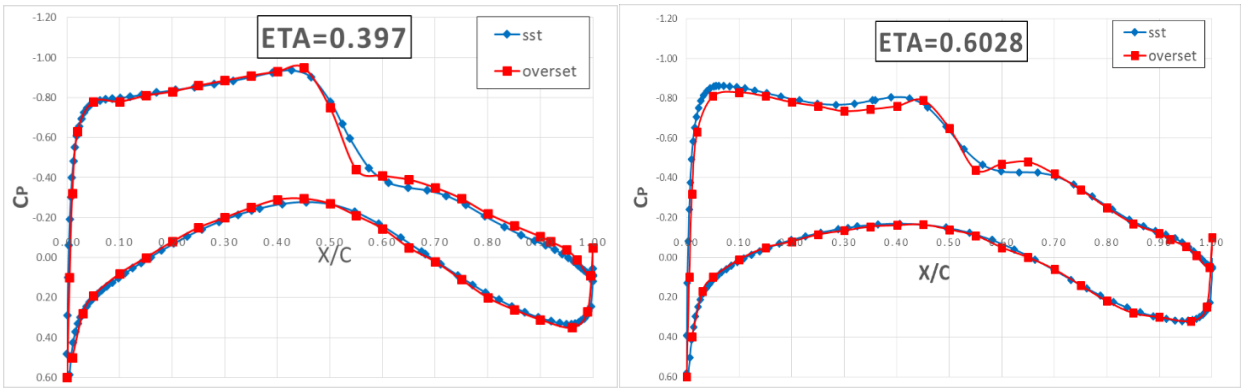

(c) (d)

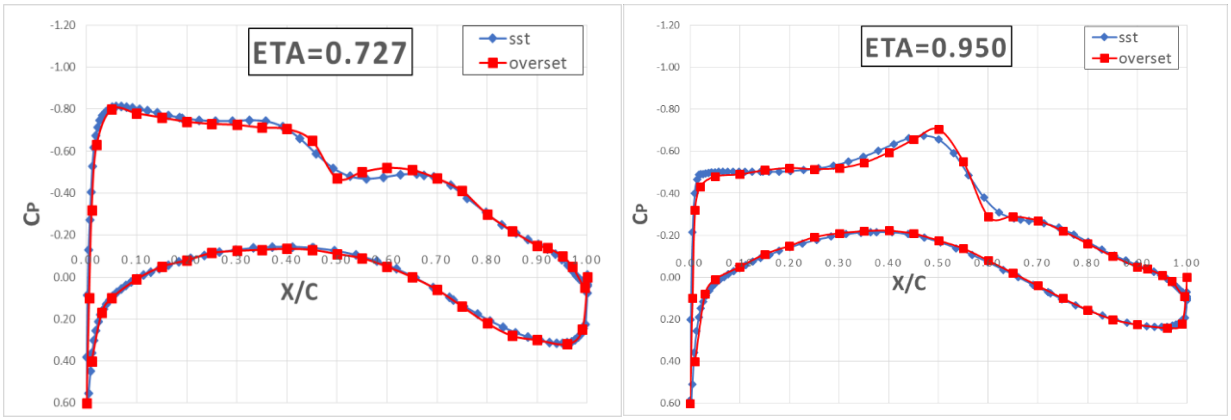

(e) (f)

Fig 4.2 Pressure distribution at several cross sections of the wing of WBPN

Figure 4.3 shows the pressure contours on WBNP. Figure 4.3 (a) shows the three-dimensional view. Figure 4.3 (b) and 4.3 (c) show the view in -z and +z direction respectively. It can be noted that the general pressure distribution is similar to that in the WBT configuration. The pressure on the wing is certainly affected by the existence of nacelle and pylon. The area with high pressure is also located at the leading edge of the engine beside the nose of the aircraft. In addition, Fig. 4.3 (d) and 4.3 (e) show the detailed pressure distribution inside the nacelle and on the pylon. It appears that the pressure inside the nacelle wall is higher than the pressure on its outside surface. This is

caused by the compression of air flow when it travels through the nacelle. Highest pressure area is located near the stagnation points, which is exactly the leading round edge of the nacelle. The upper area of the nacelle has more negative pressure at AoA=2.75°, which means that there is more suction at the top of nacelle near the leading edge. This is similar to the negative pressure at the front part of upper face of the wing. At AoA=0°, nacelle and pylon have negative lift coefficient but at very small scale. As the AoA increases by a certain amount, these parts will also have positive lift but still on small scale. Majority of the lift comes from the wing.

Figure 4.3 (e) shows that the small area on the right side of the surface near pylon-wing juncture suffers from high pressure, which means that the high compressive strength is required at the wing pylon juncture. The small area on the left side of pylon, on the contrary, has negative pressure. This is mainly caused by the asymmetric shape of the wing and pylon. The incoming flow is rushed to the right side of the pylon-wing juncture corner, which leads to high pressure in that area leaving other side of the pylon at negative pressure.

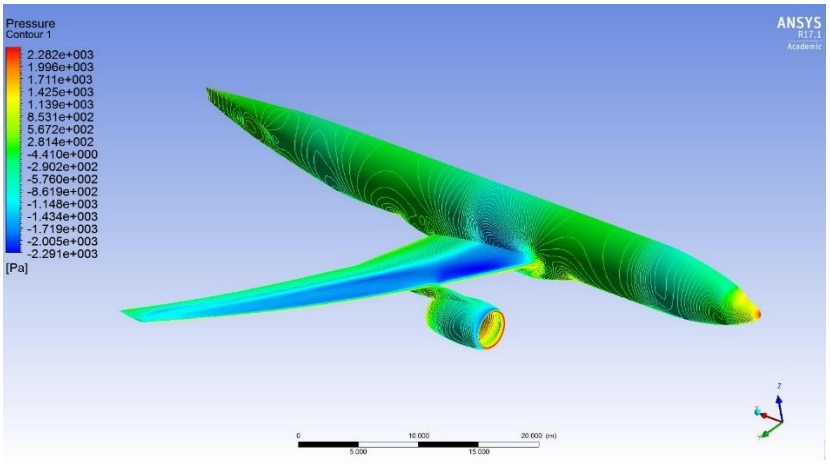

(a) 3D pressure contours on the WBNP configuration

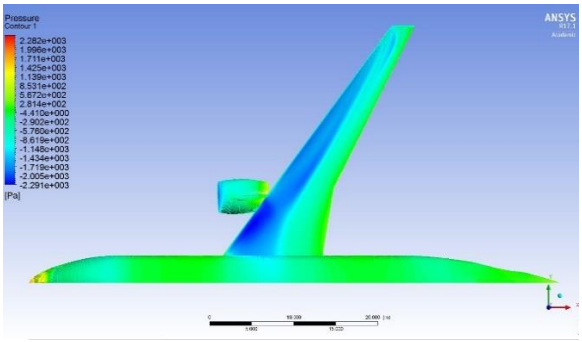

(b)

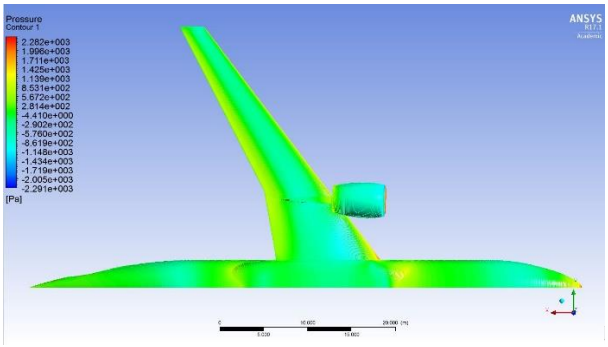

(c)

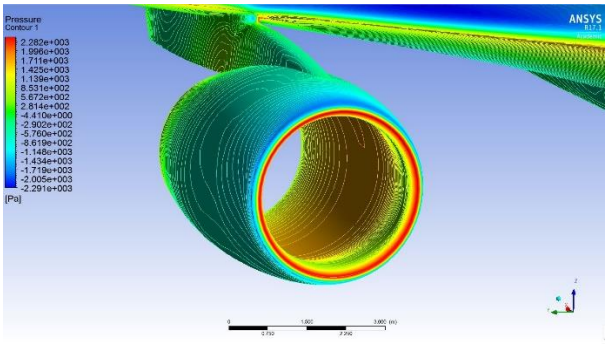

(d)

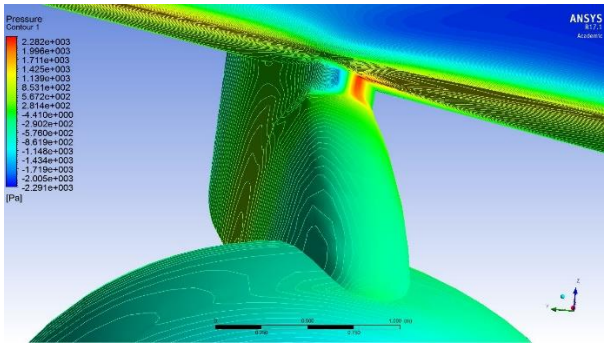

(e)

Fig 4.3 Computed pressure contours on WBNP using ANSYS FLUENT with SST k-ω model

4.3 Pressure Distribution on Nacelle Cross-Sections

Figure 4.4 shows six cross-sections on the nacelle equally divided into six parts where pressure distributions computed from FLUENT with SST k-ω model are compared with the computation given on the DPW6 website [15].

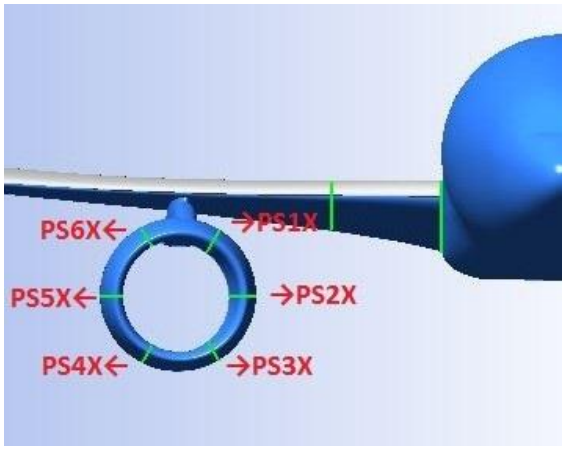

Fig 4.4 Six cross-sections on the nacelle

Figure 4.5 shows the comparison of computed pressure distribution using FLUENT with SST k-ω model and the benchmark results reported at the DPW6 website [15]. By comparing cross section PS1X and PS6X, although two sections are in symmetry position referring to the nacelle, the suction is more obvious in PS6X than that in PS1X. This is consistent with the pressure distribution at pylon-wing juncture. As to the accuracy of the nacelle pylon pressure distribution, the overall shape is consistent between the present SST k-ω model results and computational results from DPW6.

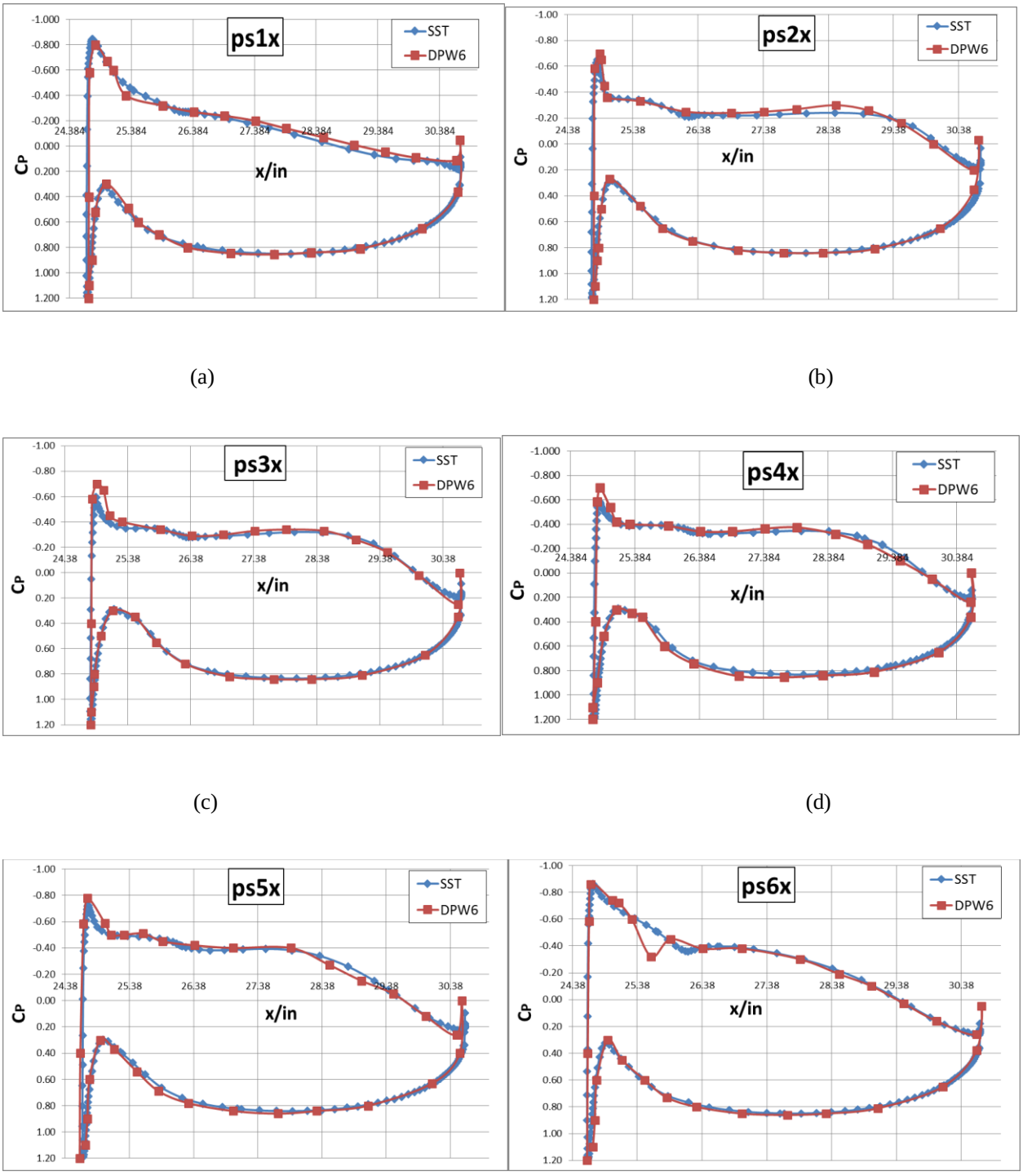

Fig 4.5 Pressure distributions on six cross-sections of nacelle

4.4 Conclusions

In conclusion, at AoA=2.75°, the present drag and lift coefficient results obtained with SA and SST k-ω models are in close agreement with the FUN3D results published in DPW6. When compared to the experimental result, it appears that there still exists small error between the simulation results and the experimental results. The error is more obvious in the figure of idealized drag polar, which can again be explained by the difference in wind tunnel conditions and the computational model.

The pressure distributions on the wing of WBNP computed using Fluent with SST k-ω model and Overset results are in good agreement. The magnitude of pressure at most X coordinates are almost the same. The shock location is generally the same. However, small error is observed at the center of the wing, but it is within reasonable range.

For Nacelle pressure distributions, the overset results and present results using Fluent with SST k-ω model are close to each other. At the leading edge of nacelle, the outer surface pressure distribution is a little bit different between the two results. It appears that Fluent results with SST k-ω model didn't accurately capture the rapid change in pressure, but still, they are within reasonable range. From the shape of the pressure curves, one can see that the nacelle is experiencing an extensive force due to the flow. The pylon has significantly different pressure around the pylon wing juncture. The side facing the fuselage has high pressure but the other side has negative pressure. This is caused by the nature of the geometry of the wing and pylon.

Chapter 5: Drag Increment Study

This chapter describes the results of drag increment study for the aeroelastic wing-body model WBae2.75.

5.1 Lift and Drag Coefficients and Drag Polar of WB Ae2.75

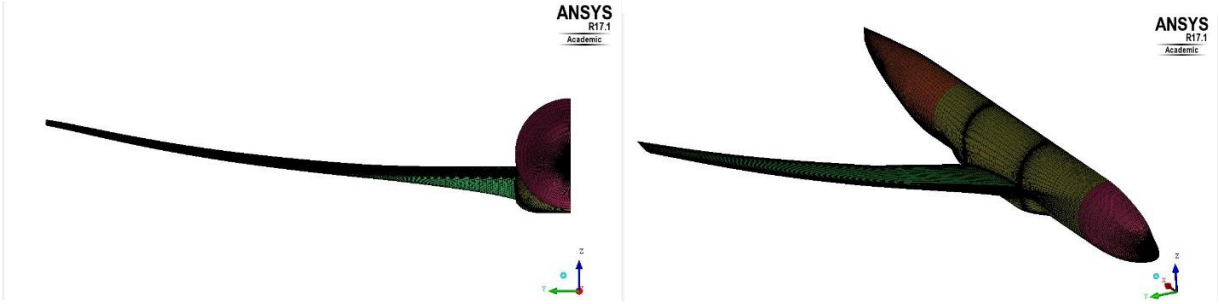

(a) (b)

Figure 5.1 Aeroelastic geometry and mesh

Comparison of drag and angle of attack under the condition of C_d=0.5000 for WB and WBNP common research models is required in DPW6. Both models take into account the aeroelasticity of wing deformation. Previous results have already shown the drag coefficient vs. angle of attack curve for WBNP. Figure 5.2 shows the result for WB configuration and its comparison with WBNP using the SST k-ω model. Figure 5.1 shows the deformation of the wing and the mesh shells on the model. To clearly observe the shock location and pressure distribution, the O grind

around the wing tip and the edges is made extra dense for higher accuracy.

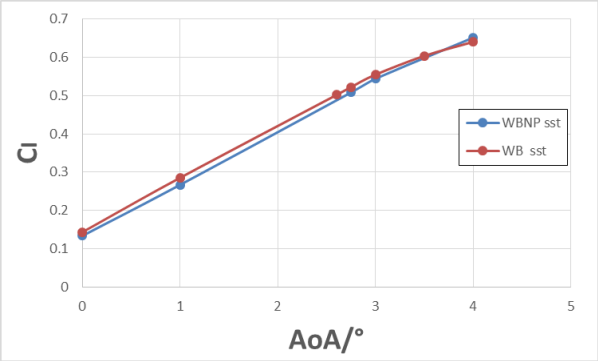

(a) Lift coefficient vs. angle of attack

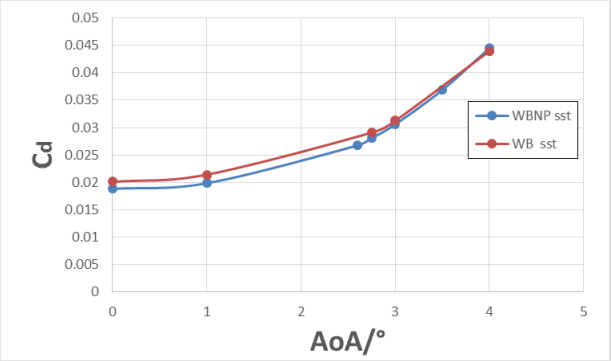

(b) Drag coefficient vs. angle of attack

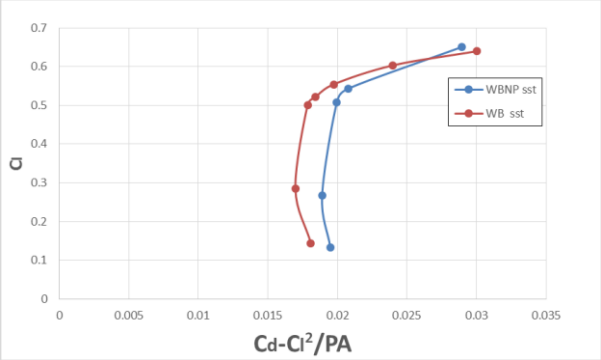

(c) Idealized drag polar

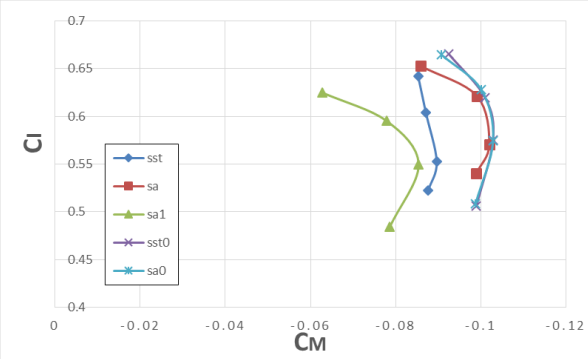

(d) Pitching moment

Fig 5.2 Drag, lift and Pitching moment curves

As shown in Fig. 5.2, the drag coefficient of WB model is generally less than that of WBNP with nacelle and pylon, while the lift coefficient is higher. Furthermore, the skin friction on nacelle and pylon add more drag WBNP compared to WB. The pylon and nacelle interrupt the flow approaching the wing causing the development of a vortex surface at the wing-pylon juncture and creating a positive pressure distribution on the lower surface of the wing. At higher angle of attack (especially when α >= 3°), the lift coefficient vs. angle of attack curve appears to have a decreasing trend in WB. It seems that the flow separates on the upper surface of the model to

decrease the lift at high angle of attack. As shown in Figure 5.2 (d), the 'blue' and 'red' points are simulation results using the SST k-ω and SA model respectively obtained by the author of this thesis. Other curves come from the data collected from DPW6. The pitching moments from all numerical simulations exhibit a decreasing and increasing trend for AoA=2.75° to 4°. This is due to separation near the trailing edge of the wing causing the nose-up pitching moment to decrease, which leads to the increase in the total pitching moment. In general, all simulation results are in good agreement.

5.2 Comparison of Drag between WB and WBNP for Ae2.75

Table 5.1 Geometry information for WB and WBNP

	α	C_l	C_d
WB	2.59	0.50032	0.026651
WBNP	2.71	0.50097	0.028536
Increment%	4.6332		7.0741

The comparison of drag for WB and WBNP is conducted under the same conditions. Here, the lift coefficient is limited to C_l=0.5±0.001. Table 5.1 shows the comparison between the lift and drag coefficients of WB and WBNP. From Table 5.1 one can clearly see that the increment in angle of attack is about 4.6332%, and in drag coefficient is about 7.0741% in WBNP compared to WB for the same lift. With nacelle and pylon, it takes more inclination to reach the same level of lift force. Figure 5.3 shows the pressure distributions on WB and WBNP.

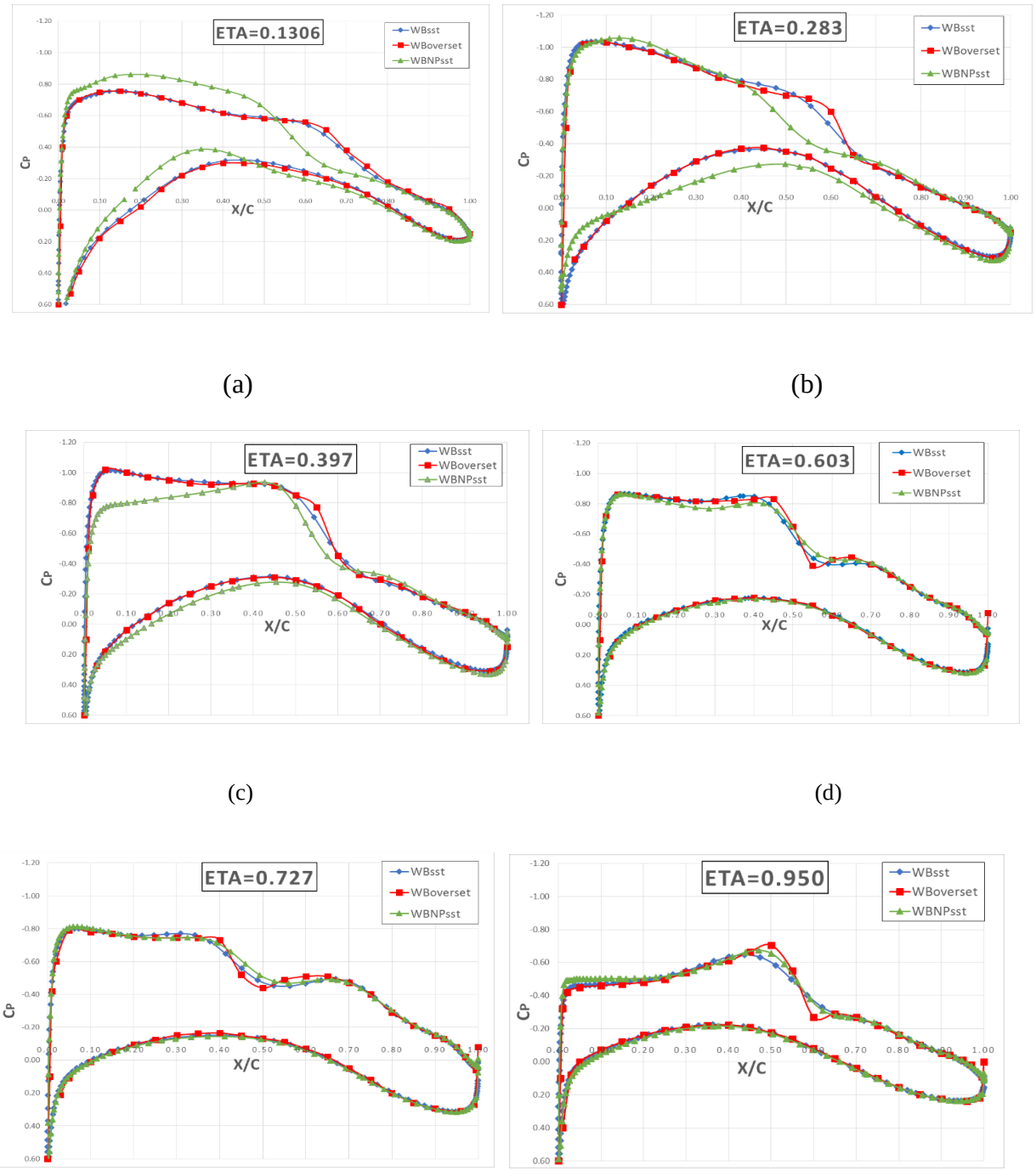

Fig 5.3 Pressure distribution on various wing sections for WB and WBNP at AOA=2.59°

As shown in Fig 5.3, by comparing the results of WB with SST k-ω model and WB overset results. One can conclude that two sets of computational results match quite well overall. At ETA=0.95,

the two results have some difference on the middle part of the upper surface of the wing. The shock shapes are not exactly alike.

By comparing the WB results with SST k-ω model and WBNP results with SST k-ω model, it appears that the difference mainly exists at ETA=0.397 and 0.283. These two sections are located closest to the nacelle and pylon with respect to Y axis. With nacelle and pylon, the shape of the pressure curve on the lower surface of the wing changes. The point of maximum pressure on the upper surface of the wing moves towards the trailing edge when nacelle and pylon are added.

Another phenomenon that should be noticed is that there is always error at around x/c=0.5 on the wing in the pressure distributions from different simulation results for both WBNP and WB configurations, which is shown in Fig. 4.2 & Fig. 5.3. This results due to complex flow pattern near the middle part of the wing, where the shock near the leading edge just ends and interacts with the boundary layer on the upper surface of the wing. The solution of flow field in these areas is sensitive to the grid quality, type of solver and turbulence models. As a result, it is possible that the error will always exist at the middle of the wing in different simulation cases; however, the errors are within acceptable range.

5.3 Separated flow on Wing-Body Configuration at Various Angles of Attack using SST k-ω and SA Model

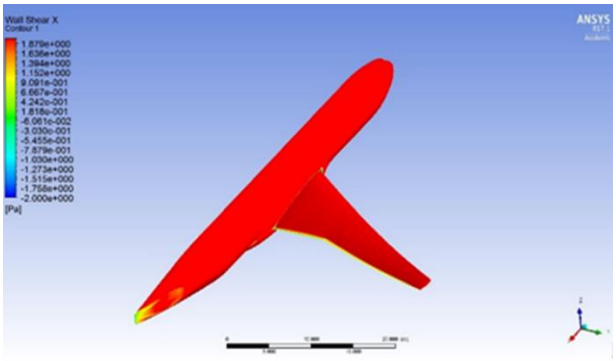

(a) AoA=2.75° (SST)

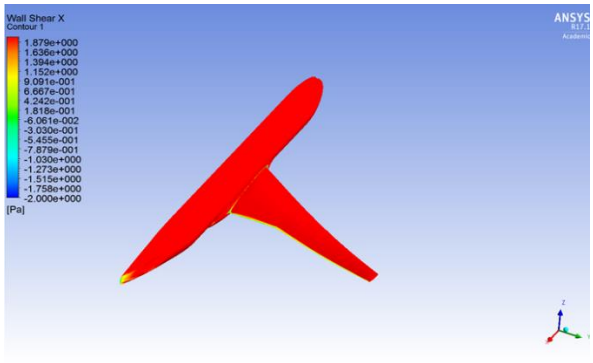

(b) AoA=2.75° (SA)

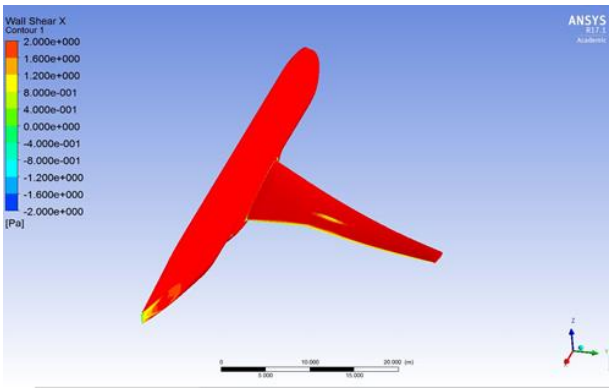

(c) AoA=3.00° (SST)

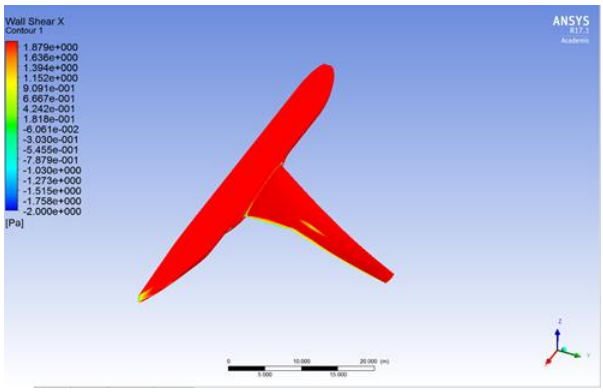

(d) AoA=3.00° (SA)

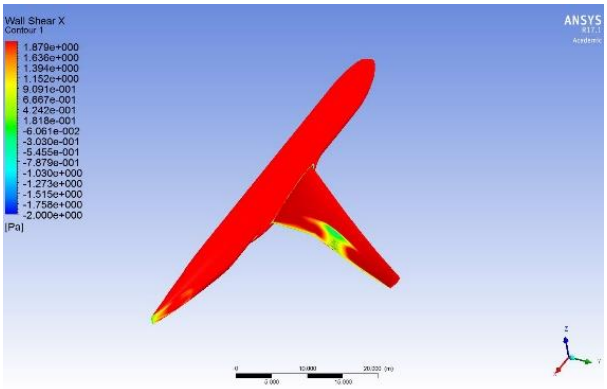

(e) AoA=3.50° (SST)

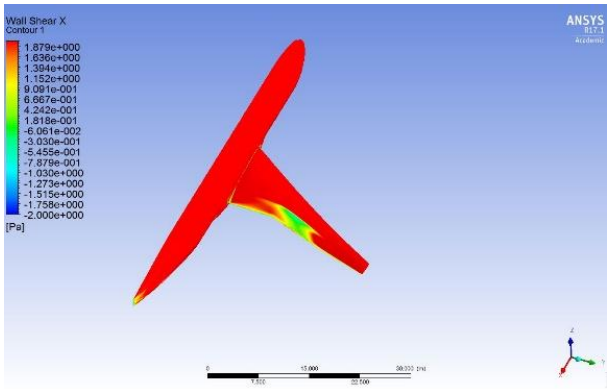

(f) AoA=3.50° (SA)

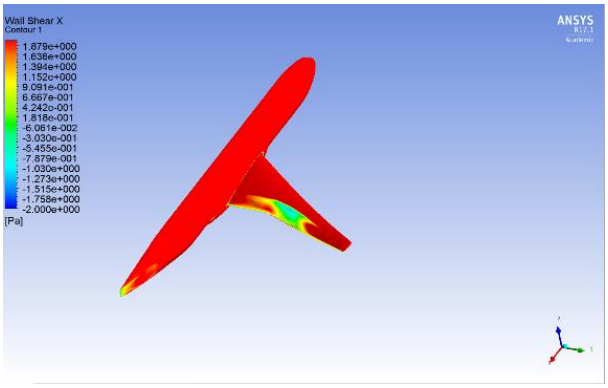

(g) AoA=4.00° (SST)

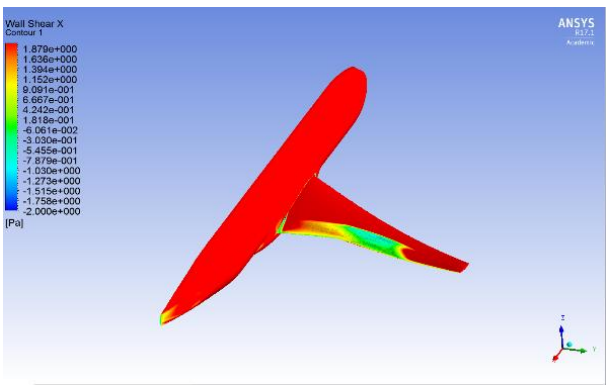

(h) AoA=4.00° (SA)

Fig 5.4 $C_{f,x}$ for Wing-Body configuration for various angles of attack using the SST k-ω and SA model

Fig. 5.4 shows the wall shear stress in the X axis direction. At AoA=2.75° and 3.00 °, there is primarily flow separation from the wing root near the trailing edge (SOB separation). At AoA= 3.50 ° and 4°, the flow separation appears at the center of the upper surface of the wing, which is called the trailing edge separation (TE separation). It grows as angle of attack becomes higher, which explains the decrease in lift as the angle of attack becomes larger. It should be noted that the flow separation region computed by the SA model is higher than that computed by the SST k-ω model.

5.4 Conclusions

In conclusion, the lift and drag coefficients computed using the SST k-ω and SA model are in close agreement. When one compares the WBNP ae 2.75 and WB ae 2.75 results, at the same angle of attack, the lift force on WB is higher than that on WBNP. The nacelle and pylon in WBN reduce the lift.

The addition of nacelle and pylon leads to increment in drag for the same lift coefficient. To achieve the same lift for WB, the WBNP configuration must have a higher angle of attack. When

observing the pressure distribution on the wing, one can conclude that the pressure distribution on the wing near the nacelle is different in WBNP compared to WB; the pressure on the lower surface of wing changes significantly. At ETA=0.397, the maximum pressure point moves toward the center of the wing after nacelle and pylon are added.

For WB, the skin friction in X axis direction is computed to determine the flow separation region on the wing. At AoA=2.75°, the separation is obvious at the wing fuselage juncture. As the angle of attack increases, separation begins to appear at the center of the wing. This explains why the increase in the angle of attack beyond AOA=3.0° results in decrease in the lift. Also, it can be seen from Fig. 5.4 that the separation region computed by the SA model is larger than that computed by the SST k-ω model on the WB configuration at the same angle of attack.

Chapter 6 Conclusions

The flow fields of two NASA common research models (WBT and WBNP) are investigated by numerical simulations using ANSYS FLUENT by solving the RANS equations with SA and SST *k-ω* turbulence models. The computations are compared with benchmark computations reported on the AIAA DPW4 and DPW6 websites and with the experimental data where available. Overall, good agreement is obtained with the results reported in the literature for both the configurations.

For WBT configuration, some discrepancy was found between the computed results and the experimental data at higher angle of attack of α = 4°; there is flow separation near the trailing edge of the wing-body juncture at this angle of attack. The present results from ANSYS FLUENT with SST k-ω model agree well with those from NASA OVERFLOW code using the SA model. For the pitching moment, all pitching moment curves show decreasing and increasing trend as the angle of attack increases. Results from DPW4 match well with the results obtained in this thesis. For WBNP configuration, the computed lift and drag are in acceptable agreement with the experimental results. Computational results are generally consistent with other computational results in DPW6, except some details of shock shapes are different. However, the error is acceptable. The WBNP results can be improved by using a finer mesh as recommended on the DPW 6 website.

For the drag increment study, the effect of nacelle and pylon on increasing the drag can be clearly seen. Both the angle of attack and drag coefficient increase as nacelle and pylon are added to the wing-body configuration for maintaining the same lift. Comparing the flow field of WB and WBNP, it can be seen that the pressure distributions at cross sections near the fuselage change due to the presence of nacelle and pylon. Pitching moment for WB configuration in all simulations

are in good agreement with the computations of other investigators. The flow separation is detected at the center of the wing of WB configuration which leads to decrease in of lift as the angle of attack increases. Computations with both SA and SST turbulence models predict increase in trailing edge (TE) separation as the angle of attack increases. SA model computes larger separation region on the wing compared to the SST k-ω model at same angle of attack.

References

1. Anthony J. Sclafani and John C. Vassberg, "Analysis of the Common Research Model Using Structured and Unstructured Meshes," *Journal of Aircraft*, Vol. 51, No. 4, July–August 2014, pp.1223-1243, doi: 10.2514/1.C032411

2. Stefan Keye, Olaf Brodersen, and Melissa B. Rivers, "Investigation of Aeroelastic Effects on the NASA Common Research Model," *Journal of Aircraft*, Vol. 51, No. 4, July–August 2014, pp.1323-1330, doi: 10.2514/1.C032598

3. E. M. Lee-Rausch, D. P. Hammond, E. J. Nielsen, S. Z. Pirzadeh, and C. L. Rumsey, "Application of the FUN3D Solver to the 4th AIAA Drag Prediction Workshop," *Journal of Aircraft*, Vol. 51, No. 4, July–August 2014, pp.1149-1160, doi: 10.2514/1.C032558

4. Anthony J. Sclafani, Mark A. DeHaan, and John C. Vassberg, "Drag Prediction for the Common Research Model Using CFL3D and OVERFLOW," *Journal of Aircraft*, Vol. 51, No. 4, July–August 2014, pp.1101-1117, doi: 10.2514/1.C032571

5. Joseph H. Morrison, "Statistical Analysis of the Fourth Drag Prediction Workshop Computational Fluid Dynamics Solutions," *Journal of Aircraft*, Vol. 51, No. 4, July–August 2014, pp.1090-1100, doi: 10.2514/1.C032737

6. Mori Mani, Ben J. Rider, Anthony J. Sclafani, Chad Winkler, John Vassberg, Andrew J.Dorgan, Andrew Cary, and Edward N. Tinoco, "Reynolds-Averaged Navier–Stokes Technology for Transonic Drag Prediction: A Boeing Perspective," *Journal of Aircraft*, Vol. 51, No. 4, July–August 2014, pp.1118-1134, doi: 10.2514/1.C032717

7. John Vassberg, et al. "Development of a Common Research Model for Applied CFD Validation Studies," AIAA paper 2008-6919, *26th AIAA Applied Aerodynamics Conference*, 2008.

8. Marco Osward, ANSYS Germany GmbH, "4th AIAA CFD Drag Prediction Workshop," https://aiaa-dpw.larc.nasa.gov/Workshop4/presentations/DPW4_Presentations_files/D1-9_DPW4-ANSYS-Marco-Oswald-new.pdf

9. P. R. Spalart and S. R. Allmaras, "A One-Equation Turbulence Model for Aerodynamic Flows," AIAA Paper 92-0439, Jan. 1992.

10. Florian R. Menter, "Two-Equation Eddy-Viscosity Turbulence Models for Engineering Applications," AIAA Journal, Vol. 32, No.8, 1994, pp.1598–1605, Bibcode:1994 AIAA J..32.1598M, doi:10.2514/3.12149

11. John C. Vassberg, Edward N. Tinoco, Mori Mani, Ben Rider, Tom Zickuhr, David W. Levy, Olaf P. Brodersen, Bernhard Eisfeld, Simone Crippa, Richard A. Wahls, Joseph H.

Morrison, Dimitri J. Mavriplis and Mitsuhiro Murayama, “Summary of the Fourth AIAA Computational Fluid Dynamics Drag Prediction Workshop,” *Journal of Aircraft*, Vol. 51, No. 4, July–August 2014, pp.1070-1089, doi: 10.2514/1.C032418

12. Melissa B. Rivers, and Ashley Dittberner, “Experimental Investigations of the NASA Common Research Model,” *Journal of Aircraft*, Vol. 51, No. 4, July–August 2014, pp.1183-1193, doi: 10.2514/1.C032626

13. Khaled S. Abdol-hamid, Chris Rumsey, Jan Carlson, and Mike Park, NASA Langley Research Center, Hampton, VA, June 2016, https://aiaa-dpw.larc.nasa.gov/Workshop6/presentations/2_02_DPW6_Pres_CLR8.pdf

14. Brain A. Edge, Metacomp Technologies, Inc., Summary of Results from the CFD++ Software Suite, https://aiaa-dpw.larc.nasa.gov/Workshop6/presentations/1_12_MetacompTechnologies.pdf

15. Ed Tinoco, and Olaf Brodersen, the DPW Organizing Committee, Washington D.C.June /2016,https://aiaa-dpw.larc.nasa.gov/Workshop6/presentations/2_10_DPW6_Summary-Draft-ET.pdf

Vita

Pan Du

Degrees M.S. Mechanical Engineering, May 2017
B.S. Thermal Engineering, June 2015

Birth of Place Yulin, Shaanxi, China

Publications Pan Du and Ramesh K. Agarwal, "Drag Prediction of NASA Common Research Models Using Different Turbulence Models,"

35th AIAA Applied Aerodynamics Conference, Denver, Colorado, 5-9 June 2017.

May 2017